


Cite this: *RSC Adv.*, 2017, 7, 50040Received 9th September 2017  
Accepted 12th October 2017

DOI: 10.1039/c7ra10060d

rsc.li/rsc-advances

# The controllable fabrication of a novel hierarchical nanosheet-assembled Bi<sub>2</sub>MoO<sub>6</sub> hollow micronbox with ultra-high surface area for excellent solar to chemical energy conversion†

Chunjing Shi, Xiaoli Dong, \* Yuchen Hao, Xiuying Wang, Hongchao Ma and Xiufang Zhang

Herein, we demonstrated for the first time the fabrication of a novel nanosheet-assembled Bi<sub>2</sub>MoO<sub>6</sub> micronbox *via* a simple one-step method. In particular, this new Bi<sub>2</sub>MoO<sub>6</sub> framework structure with ultra-large surface area can endow the sample with strong light harvesting ability and abundant surface active sites and it exhibits remarkably enhanced photocatalytic activity toward organic dye degradation and nitrogen fixation under solar-light irradiation, far exceeding that of conventional Bi<sub>2</sub>MoO<sub>6</sub> with a different structure.

To date, the increasingly serious energy crisis and environmental pollution have attracted extensive interest in society. Photocatalytic solar energy conversion has been investigated as promising and sustainable green technology for solving the aforementioned problems.<sup>1</sup> Notably, semiconducting oxides as catalysts are indispensably promising candidates.<sup>2</sup> However, the high efficiency of the photocatalyst is mainly determined by three processes: optical absorption, charge separation and migration, and the catalytic reaction on the surfaces.<sup>3</sup> Nonetheless, these factors are limited by the band gap, morphology, active sites of the photocatalysts, *etc.*<sup>4</sup> It is of particular note that the morphology of the photocatalyst is one of the most crucial factors in improving the photocatalytic property. For this reason, the separation rate of the photoinduced surface and volume charge carriers in a photocatalyst can be significantly increased by assembling or integrating to control their shape and the structure of their primary building blocks. As a result, the photocatalytic activity can observably improve among the variety of semiconductors studied.<sup>5</sup> In view of this, the quest for highly efficient and practical light-driven photocatalysts with appropriate morphology is greatly crucial and a huge challenge.

Initially, we must carefully select a suitable semiconductor that can be regarded as an indispensable basis-material. As is known, over the past few decades, titanium dioxide (TiO<sub>2</sub>) in

various structures has been investigated with respect to its potential as a catalyst for photochemical applications.<sup>6</sup> However, TiO<sub>2</sub> structures have a drawback in their ability to only absorb light in the UV and near-UV regions due to their high band gap (~3.2 eV).<sup>7</sup> This results in an open problem for investigation because solar light consists of 4% UV light, 43% visible light, and the near-infrared region making up the rest,<sup>8</sup> and consequently solar energy cannot be completely harvested on a TiO<sub>2</sub> semiconductor surface. To overcome insufficient solar light utilization, there is significant interest in exploring visible-light-sensitive photocatalysts. In combination with optical trapping, the controlled fabrication of hierarchical intercrossed frameworks could serve as an alternative strategy for further improving the photocatalytic performance.<sup>9</sup>

Thus, as a new kind of nontoxic photocatalyst, bismuth molybdate (Bi<sub>2</sub>MoO<sub>6</sub>) has drawn increasing attention in photocatalytic pollutant degradation, water oxidation, and CO<sub>2</sub> reduction due to its proper band gap energy and high chemical stability.<sup>10</sup> In this work, we demonstrated that a nanosheet-assembled Bi<sub>2</sub>MoO<sub>6</sub> micronbox with ultra-large surface area achieved efficient sunlight-driven degradation of organic dyes/nitrogen fixation under light irradiation.<sup>11</sup> In particular, the novel mesoporous structure and large surface area can endow the sample with a strong light harvesting ability and an abundance of surface active sites. In addition, the ultra-small subunits can efficiently suppress bulk charge recombination between the photo-generated electrons and holes *via* the shortening carrier transfer distance from the inner to the catalyst surface. As a surprising achievement, the as-prepared sample exhibits excellent photocatalytic performance compared with a conventional large-sheet Bi<sub>2</sub>MoO<sub>6</sub> photocatalyst. The novel mesoporous structure was regarded as one of

School of Light Industry and Chemical Engineering, Dalian Polytechnic University, #1 Qinggongyuan, Dalian 116034, P. R. China. E-mail: dongxi@dlpu.edu.cn

† Electronic supplementary information (ESI) available: Detailed experimental section, synthetic mechanism, photocatalytic activity test of the B-Bi<sub>2</sub>MoO<sub>6</sub> samples, SEM and EDS images of the B-Bi<sub>2</sub>MoO<sub>6</sub> samples, high resolution Bi 4f, O 1s and Mo 3d XPS spectra of B-Bi<sub>2</sub>MoO<sub>6</sub>, UV-vis diffuse reflectance spectra, Tauc plots of the as-prepared samples, VB XPS spectra, and PL spectra. See DOI: 10.1039/c7ra10060d



the most influential reasons restricting the potential photocatalytic activity due to its intrinsic specific surface area and internal construction.

In brief, using a simple one-step method, a novel nanosheet-assembled  $\text{Bi}_2\text{MoO}_6$  micronbox was fabricated successfully for the first time. We employed conventional and low cost reagents as reactants to achieve the assembled building blocks. The as-prepared samples were characterized by a variety of characterization techniques. The sunlight-driven pollutant degradation and nitrogen fixation performance were measured under simulated sunlight or visible light irradiation at room temperature. The characterization details and photocatalysis conditions can be found in the ESI.† The crucial synthetic mechanism of the as-prepared B- $\text{Bi}_2\text{MoO}_6$  is provided in Fig. S1†, and a detailed explanation is provided in the schematic illustration of the synthetic mechanism.

To observe the macroscopic and subtle structure of the as-prepared  $\text{Bi}_2\text{MoO}_6$  micronbox, SEM and TEM images were obtained. As shown in Fig. 1a and b, the resultant sample possesses a box-like morphology and multi-level hierarchical structure. In addition, from the inset of Fig. 1a, we can clearly see that the micronbox consisted of many nanosheets that were several nanometers thick, and the cross-linking of the nanosheets formed a novel mesoporous structure. The SEM images comparing C- $\text{Bi}_2\text{MoO}_6$  and the other four samples with different shapes are presented in Fig. S2 and S3.† The TEM images (Fig. 1c and d) further confirm the ultrathin nanosheet assembled box-like morphology of the as-prepared sample. The obvious contrast between the dark edge and bright center indicates that the as-prepared sample possesses a hollow structure.<sup>12</sup> Therefore, this evidence could intuitively prove the formation of the hierarchical and hollow nanosheet-assembled micronbox.

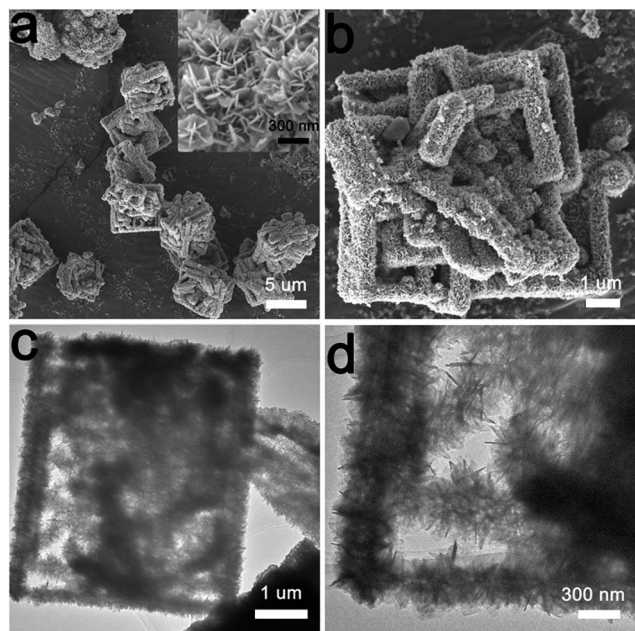


Fig. 1 (a and b) The FESEM images of B- $\text{Bi}_2\text{MoO}_6$  (inset: a high-magnification SEM image); (c and d) the TEM images of B- $\text{Bi}_2\text{MoO}_6$ .

Beyond this, the EDX mapping images of the as-prepared sample reveal a uniform distribution of the Bi, O and Mo elements throughout the material (Fig. 2a–d and S4†), suggesting the successful synthesis of the pure phase  $\text{Bi}_2\text{MoO}_6$  catalyst. To better verify this conclusion, more sufficient evidence extracted from the XRD patterns and XPS analysis was obtained. As shown in Fig. 2e and S5,† the distinct diffraction peaks of the different samples at  $28.3^\circ$ ,  $32.9^\circ$ ,  $47.0^\circ$ ,  $56.0^\circ$ ,  $58.5^\circ$ , and  $68.8^\circ$  correspond to the (131), (002), (062), (133), (262), and (400) crystal planes of orthorhombic  $\text{Bi}_2\text{MoO}_6$  (JCPDS 84-0787), respectively. In addition, no other diffraction peaks from impurities can be found, indicating that the as-prepared samples possessed high purity.<sup>13</sup> Furthermore, the X-ray photoelectron spectroscopy (XPS) full-scan analysis of B- $\text{Bi}_2\text{MoO}_6$  presents the Bi, O, and Mo elements of the samples (Fig. 2f). For the high-resolution Bi 4f spectrum, the obvious peaks at 157.96 eV ( $\text{Bi } 4f_{7/2}$ ) and 162.92 eV ( $\text{Bi } 4f_{5/2}$ ) can be ascribed to  $\text{Bi}^{3+}$  in the crystal structure (Fig. S6†).<sup>14</sup> Additionally, the Mo 3d peaks centered at 231.9 eV and 235.0 eV can be ascribed to Mo  $3d_{5/2}$  and Mo  $3d_{3/2}$ , respectively (Fig. S7†). Moreover, the high resolution O 1s spectrum (Fig. S8†) shows the lattice oxygen and adsorbed oxygen at 530 eV and 532.5 eV, respectively. As a result, the above analyses fully confirmed that the pure phase  $\text{Bi}_2\text{MoO}_6$  catalyst was synthesized *via* the solvothermal route.

On the other hand, the nitrogen sorption isotherm of the as-prepared B- $\text{Bi}_2\text{MoO}_6$  possesses an obvious condensation step around  $P/P_0 = 0.5$ – $0.9$ , and it has hysteresis loops that are typical of mesoporous materials (Fig. 3a). This therefore

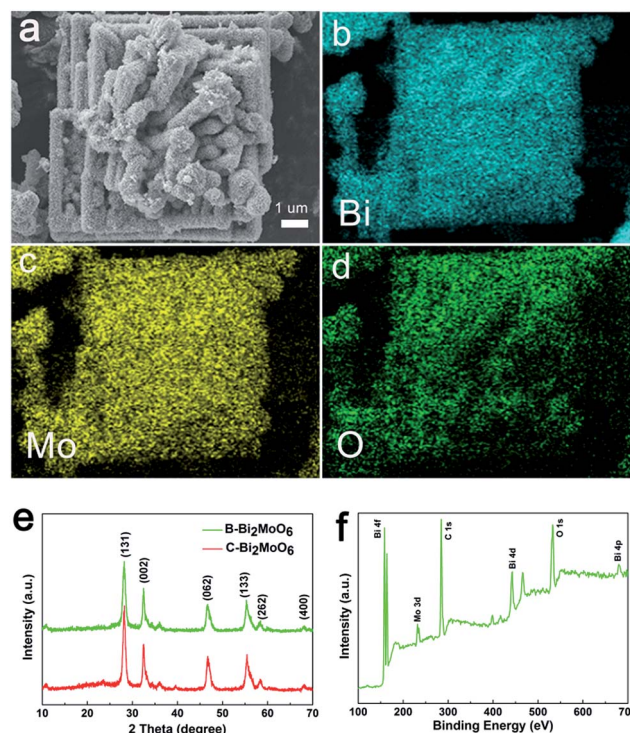


Fig. 2 (a–d) A typical EDS elemental mapping of B- $\text{Bi}_2\text{MoO}_6$  (Bi, Mo, O); (e) the XRD patterns of B- $\text{Bi}_2\text{MoO}_6$  and C- $\text{Bi}_2\text{MoO}_6$ ; (f) the XPS spectra of B- $\text{Bi}_2\text{MoO}_6$ .



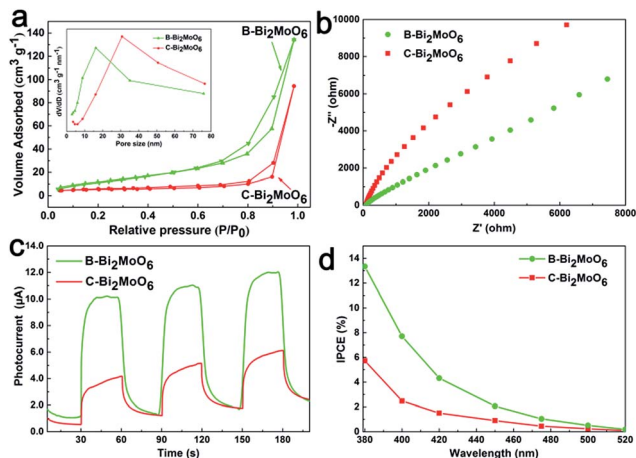


Fig. 3 (a) The  $N_2$  sorption isotherm and pore size distributions (inset) of B- $Bi_2MoO_6$  and C- $Bi_2MoO_6$ ; (b) the EIS Nyquist plots of the as-prepared M- $Bi_2MoO_6$  and C- $Bi_2MoO_6$ ; (c) the photocurrent–time ( $I-t$ ) curves of the obtained B- $Bi_2MoO_6$  and C- $Bi_2MoO_6$ ; (d) the incident photon to current efficiency (IPCE) curves.

indicates that the as-prepared B- $Bi_2MoO_6$  possesses a mesoporous structure, while the conventional  $Bi_2MoO_6$  does not possess an obvious porous structure. In addition, B- $Bi_2MoO_6$  exhibits an ultra-large surface area ( $54.56 \text{ cm}^2 \text{ g}^{-1}$ ), which is more than 3 times larger than that of C- $Bi_2MoO_6$ . The novel mesoporous structure and ultra-large surface area can not only promote the diffusion of the active species and accelerate the subsequent surface reactions, but they can also provide more surface active sites for oxygen activation and reduction, and thereby positively facilitate the reaction process and endow the catalyst with robust redox kinetics.

For sunlight-driven photocatalysis, efficient solar energy harvesting and carrier separation are very important, which are the preconditions for future energy coupling between excitons and ammonia. To better depict this process, firstly, the light-harvesting performance was investigated. As indicated by the UV-vis diffuse reflectance spectrum (Fig. S9†), after assembly of the  $Bi_2MoO_6$  nano-sheets into a mesoporous box-like structure, the light harvesting ability was further enhanced. By contrast, we can suggest that the excellent optical absorption performance of B- $Bi_2MoO_6$  was mainly due to two main aspects. One is the large light contact areas, which mean that more photons can be absorbed by B- $Bi_2MoO_6$  and thus generate more excitons to take part in the redox reaction. The other is the robust light scattering in the specific mesoporous hollow structure, which means an increase of the optical path length of the incident light to promote light absorption. Additionally, valence-band (VB)-XPS (Fig. S11†) combined with the corresponding Tauc plot analysis (Fig. S10†) is a method to determine the conduction band (CB) and VB positions. We can estimate that the CB position of B- $Bi_2MoO_6$ , based on the band gaps, was  $-1.35 \text{ vs. the normal hydrogen electrode}$ . Based on the CB positions of the B- $Bi_2MoO_6$  analysis, it can be seen that the CB positions of the B- $Bi_2MoO_6$  sample are higher than  $E_0 (N_2/NH_3 = -0.28 \text{ V vs. NHE})$ . Hence, the as-prepared samples not only possess

powerful photocatalytic performance of dye degradation, but they can also efficiently reduce nitrogen to generate ammonia.

Besides this, photoluminescence spectroscopy (PL; Fig. S12†) and electrochemical impedance spectroscopy (EIS; Fig. 3b) were also conducted, and we have seen that the PL spectra of B- $Bi_2MoO_6$  could convincingly prove lower carrier recombination. Similarly, the radius of each arc on the EIS Nyquist plot reveals the charge transfer process occurring at the contact interface between the electrode/electrolyte interface, and the smaller radius represents the lower charge-transfer resistance.<sup>15</sup> This result is mainly due to the ultra-small subunits of B- $Bi_2MoO_6$ , which can efficiently shorten the pathways that minority carriers must travel and thus promote charge transfer from the inner to the catalyst surface. A benefit of the high light harvesting performance and charge separation efficiency is that the as-prepared B- $Bi_2MoO_6$  exhibits excellent photoelectric conversion efficiency. Fig. 3c clearly reveals that the time-dependent photocurrent measurements of B- $Bi_2MoO_6$  display high photocurrent density under simulated sunlight illumination, which is 3 times higher than that of C- $Bi_2MoO_6$ . This is seen to promote the separation of the photogenerated charge carriers, effectively prolonging the lifetime of the electron–hole pairs, and consequently improving the photocatalytic activity.<sup>16</sup> Moreover, the measurement of the incident photon to current conversion efficiency (IPCE) further confirmed that the as-prepared B- $Bi_2MoO_6$  can indeed efficiently convert photons into excitons, which means a greater electron supply for further nitrogen reduction reactions (Fig. 3d).

Thanks to the excellent photoelectric conversion efficiency and novel mesoporous structure, the as-prepared B- $Bi_2MoO_6$  exhibits excellent photocatalytic organic dye degradation performance under visible light/simulated sunlight irradiation and nitrogen fixation performance under simulated sunlight irradiation. Firstly, the photocatalytic behaviours were explored for the degradation of Rhodamine B (RhB) dyes under visible-light and simulated sunlight irradiation. For comparison, we presented the conventional C- $Bi_2MoO_6$  and novel mesoporous B- $Bi_2MoO_6$  as the catalysts for the photocatalytic reactions. As shown in Fig. 4a, the RhB degradation rate is close to 99%, which means complete degradation of the RhB dye in only 1 h under simulated sunlight irradiation. The as-prepared B- $Bi_2MoO_6$  reveals higher photocatalytic activity under visible light irradiation (Fig. S13†). Meanwhile, the rate constant of

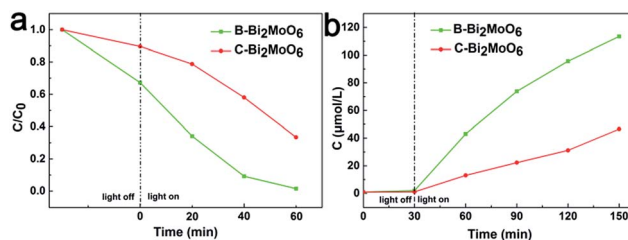


Fig. 4 (a) The degradation curves of RhB over the samples under simulated sunlight illumination; (b) the quantitative determination of the ammonia generation of the obtained samples under simulated sunlight irradiation.





degradation is presented (Fig. S14 and S15†). To investigate the stability of the as-prepared B-Bi<sub>2</sub>MoO<sub>6</sub> photocatalyst, we performed cycling experiments for photodegrading RhB over the B-Bi<sub>2</sub>MoO<sub>6</sub> photocatalyst under simulated solar illumination (Fig. S16†). According to its superiority, the as-prepared B-Bi<sub>2</sub>MoO<sub>6</sub> manifests excellent photocatalytic nitrogen fixation performance under simulated sunlight irradiation (Fig. 4b). Particularly, the ammonia generation rate gets up to 369 μmol g<sup>-1</sup> h<sup>-1</sup>, which is higher than that of the contrasted samples, after irradiation for 60 min (Fig. S17 and S18†). The AQE reaches 3.1% at λ = 380 nm and 0.15% at λ = 650 nm (Fig. S19†). Simultaneously, we enumerate the ammonia generation rate of the other reported samples in Table S1.† Such results suggest that the ultra-large surface area and novel mesoporous hollow structure can indeed achieve an unprecedented enhancement of the light-driven organic dye degradation efficiency and nitrogen fixation efficiency.

Upon gathering the above information, we identified that the novel multi-level mesoporous B-Bi<sub>2</sub>MoO<sub>6</sub> with ultra-large surface area and novel mesoporous hollow structure has significantly enhanced photocatalytic properties. The ultra-large surface area and novel mesoporous hollow structure can not only effectively facilitate charge separation and transmission but can also successfully suppress electron and hole recombination. Additionally, the unparalleled frameworks play a key role in enhancing the visible light absorption due to their unique micronbox structures and large specific surface area compared with conventional reported materials.

In summary, we undoubtedly provided a facile and simple pathway for the synthesis of Bi<sub>2</sub>MoO<sub>6</sub> with controllable structures, serving as a promising method for preparing other semiconductors. Moreover, a Bi<sub>2</sub>MoO<sub>6</sub> based light-driven pollutant decomposition and nitrogen fixation system, constructed through our optimization of the crystal structure and surface defects, can efficiently utilize solar energy and achieve energy coupling between the excitons and nitrogen. In this study, we proved that the nanosheet-built framework Bi<sub>2</sub>MoO<sub>6</sub> micronbox can efficiently degrade Rhodamine B and generate robust ammonia because of its special hierarchical porous structure, good permeability and large surface area.<sup>17</sup> It is believed that these findings could provide a new avenue to develop environmentally friendly, cheap, and efficient ammonia synthesis technology.

## Conflicts of interest

There are no conflicts to declare.

## Acknowledgements

This research was supported by the National Natural Science Foundation of China (Grant no. 21476033).

## Notes and references

- 1 Y. C. Hao, X. L. Dong, X. Y. Wang, S. R. Zhai, H. C. Ma and X. F. Zhang, *J. Mater. Chem. A*, 2016, **4**, 8298; Y. C. Hao, X. L. Dong, X. Y. Wang, H. C. Ma and X. F. Zhang, *RSC Adv.*, 2016, **6**, 102155; Y. C. Hao, X. L. Dong, X. Y. Wang, H. C. Ma and X. F. Zhang, *J. Mater. Chem. A*, 2017, **5**, 5426; C. Liu, X. L. Dong, Y. C. Hao, X. Y. Wang, H. C. Ma and X. F. Zhang, *RSC Adv.*, 2017, **7**, 22415.
- 2 Z. Y. Zhang, Y. Z. Huang, K. C. Liu, L. J. Guo, Q. Yuan and B. Dong, *Adv. Mater.*, 2015, **27**, 5906–5914.
- 3 X. B. Chen, L. Liu, P. Y. Yu and S. S. Mao, *Science*, 2011, **331**, 746.
- 4 Z. Y. Zhang, K. C. Liu, Z. Q. Feng, Y. A. Bao and B. Dong, *Sci. Rep.*, 2016, **6**, 19221.
- 5 M. Shang, W. Z. Wang, S. M. Sun, L. Zhou and L. Zhang, *J. Phys. Chem. C*, 2008, **112**, 10407.
- 6 Z. Y. Zhang, K. C. Liu, Y. A. Bao and B. Dong, *Appl. Catal., B*, 2017, **203**, 599–606.
- 7 X. B. Wei, C. L. Shao, X. H. Li, N. Lu, K. X. Wang, Z. Y. Zhang and Y. C. Liu, *Nanoscale*, 2016, **8**, 11034–11043; C. X. Wang, L. W. Yin, L. Y. Zhang, Y. X. Qi, N. Lun and N. N. Liu, *Langmuir*, 2010, **26**, 12841; D. Kannaiyan, E. Kim, N. Won, K. W. Kim, Y. H. Jang, M. A. Cha, D. Y. Ryu, S. Kim and D. H. Kim, *J. Mater. Chem.*, 2010, **20**, 677.
- 8 Z. Y. Zhang, J. D. Huang, Y. R. Fang, M. Y. Zhang, K. C. Liu and B. Dong, *Adv. Mater.*, 2017, **29**, 1606688; A. Rauf, M. Selim Arif Sher Shah, G. H. Choi, U. B. Humayoun, D. H. Yoon, J. Wook Bae, J. Park, W.-J. Kim and P. J. Yoo, *ACS Sustainable Chem. Eng.*, 2015, **3**, 2847–2855; C. J. Shi, X. L. Dong, J. W. Wang, X. Y. Wang, H. C. Ma and X. F. Zhang, *RSC Adv.*, 2017, **7**, 26717.
- 9 Y. Ma, Y. L. Jia, Z. B. Jiao, M. Yang, Y. X. Qi and Y. P. Bi, *Chem. Commun.*, 2015, **51**, 6655.
- 10 C. M. C. Vera and R. Aragona, *J. Solid State Chem.*, 2008, **181**, 1075; L. Zhou, W. Z. Wang and L. S. Zhang, *J. Mol. Catal. A: Chem.*, 2007, **268**, 195; M. S. Islam, S. Lazure, R. N. Vannier, G. Nowogrocki and G. J. Mairesse, *J. Mater. Chem.*, 1998, **8**, 655; L. W. Zhang, T. G. Xu, X. Zhao and Y. F. Zhu, *Appl. Catal., B*, 2010, **98**, 138.
- 11 W. Z. Yin, W. Z. Wang and S. M. Sun, *Catal. Commun.*, 2010, **11**, 647; J. H. Bi, L. Wu, J. Li, Z. H. Li, X. X. Wang and X. Z. Fu, *Acta Mater.*, 2007, **55**, 4699; L. W. Zhang, T. G. Xua, X. Zhao and Y. F. Zhua, *Appl. Catal., B*, 2010, **98**, 138; A. M. Beale and G. Sankar, *Chem. Mater.*, 2003, **15**, 146; H. D. Xie, D. Z. Shen, X. Q. Wang and G. Q. Shen, *Mater. Chem. Phys.*, 2008, **110**, 332; M. T. Le, W. V. Well, I. V. Driessche and S. Hoste, *Appl. Catal., A*, 2004, **267**, 227.
- 12 Y. C. Hao, X. L. Dong, X. Y. Wang, S. R. Zhai, H. C. Ma and X. F. Zhang, *Chem. Commun.*, 2016, **52**, 6525–6528.
- 13 M. Y. Zhang, C. L. Shao, J. B. Mu, Z. Y. Zhang, Z. C. Guo, P. Zhang and Y. C. Liu, *J. Mater. Chem.*, 2012, **22**, 577.
- 14 Y. S. Xu and W. D. Zhang, *Dalton Trans.*, 2013, **42**, 1094.
- 15 Y. Hou, Z. H. Wen, S. M. Cui, X. R. Guo and J. H. Chen, *Adv. Mater.*, 2013, **25**, 6291.
- 16 J. Di, J. X. Xia, S. Yin, H. Xu, L. Xu, Y. G. Xu, M. Q. He and H. M. Li, *RSC Adv.*, 2014, **4**, 14281.
- 17 X. J. Dai, Y. S. Luo, W. D. Zhang and S. Y. Fu, *Dalton Trans.*, 2010, **39**, 3426.

1 Y. C. Hao, X. L. Dong, X. Y. Wang, S. R. Zhai, H. C. Ma and X. F. Zhang, *J. Mater. Chem. A*, 2016, **4**, 8298; Y. C. Hao,

